MICROMECHANICAL SIMULATION OF A MULTIFUNCTIONAL HYBRID COMPOSITE WITH CONTINUOUS STEEL AND CARBON FIBER REINFORCEMENT

Constantin Bauer, Erik Glatt
Math2Market GmbH, Stiftsplatz 5, 67655 Kaiserslautern, Germany, www.geodict.com

Benedikt Hannemann, Sebastian Schmeer
Institute for Composite Materials (IVW GmbH), Erwin-Schroedinger-Str., Building 58, 67663 Kaiserslautern, Germany, www.ivw.uni-kl.de

Abstract

In order to understand the complex interaction of carbon and metal fibers of a loaded hybrid composite, a micromechanical model of unidirectional and multiaxial laminates is build up using the structure generators of the software GeoDict. For each constituent material, separate user defined material models (UMAT) with individual failure criterions are developed and implemented to simulate the macroscopic material behavior. Through the modelling of the microscopic structure and damages, the strength of the laminate could be determined using the solver called FeelMath which is developed at the Fraunhofer Institute for Industrial Mathematics (ITWM). This fast and memory efficient solver is capable to handle the huge number of elements required for such accurate micromechanical simulations. Additionally, the electrical conductivity of the different laminates is simulated. The numerical study is validated with experimental test investigations on unidirectional and multiaxial laminates with different steel-carbon-fiber-ratios. The obtained results are in a good accordance with the experimental data and additionally provide a detailed insight into the micromechanics of such complex hybrid composite material.

Introduction

Due to their superior mechanical properties, carbon fiber reinforced polymers (CFRP) are commonly used in lightweight applications, e.g. aviation or car industry. High structural performance to mass ratio, utilization of anisotropy for tailored strength, stiffness and stability design, excellent fatigue behavior and corrosion resistance are distinguished attributes of CFRP. However, their brittle failure behavior limits the structural integrity and damage tolerance in case of impact (e.g. tool drop, tire debris, hail strike) and crash events. To ensure the necessary robustness, a minimum skin thickness is therefore prescribed for the structure, partially exceeding stiffness and strength requirements. A minimum laminate thickness is also required to enable state-of-the-art bolted repair technologies [1]. Furthermore, the electrical conductivity of CFRP structures is insufficient for certain applications. Additional metal components are necessary to provide the electrical functionality to the structure (e.g. metal meshes for lightning strike protection in aeronautics, wires for electrical bonding and grounding, overbraiding of cables to provide electromagnetic shielding). The corresponding penalty weights compromise the lightweight potential that is actually given by the structural performance of CFRP. Former research attempts tried to overcome these deficits by modifying the resin system (e.g. by addition of conductive particles or toughening agents), but could not prove sufficient enhancements [2], [3].

A novel approach is the incorporation of highly conductive and ductile continuous metal fibers into CFRP [4]. Basic idea of this hybrid material concept is to address both the electrical and load-bearing capacities of the integrated metal fibers in order to simultaneously improve the electrical conductivity and the damage tolerance of the composite. The increased density of the hybrid material is over-compensated by omitting the need for additional electrical system installation items and by the enhanced structural performance resulting in a reduced minimum skin thickness. In this context, the present work focuses on analyzing and optimizing the structural and electrical performance of such hybrid composites. Comprehensive researches are carried out on fiber bundles as well as on unidirectional and multiaxial laminates.

Within the present study, twisted bundles of metastable austenitic chrome-nickel steel fibers (1.4301) are considered. The bundles consist of seven filaments, each with a diameter of 60 µm. Furthermore, standard modulus/high tenacity carbon fibers of type Toho Tenax HTS40 and epoxy resin of type Cytec CYCOM 977-2 are processed in terms of prepreg or resin films. Selected properties of the applied materials are summarized in table 1.

Table 1: Properties of the applied resin and fibers [5], [6]

Property	Carbon fiber [a]	Stainless steel fiber [b]	Epoxy resin [a]
Supplier	Toho Tenax	-	Cytec
Type	HTS40 F13 12k	-	Cycom 977-2
Density ρ / g/cm³	1.77	7.95 ± 0.01	1.31
Young's modulus E / GPa	240	176 ± 7	3.52
Offset yield strength $\sigma_{p0.2}$ / MPa	-	504 ± 5	-
Ultimate tensile strength σ_{max} / MPa	4300	897 ± 2	81.4
Strain at failure ε_{max} / %	1.80	32.31 ± 2.01	-
Specific electrical resistance ρ* / Ωm	1.6×10^{-5}	$(6.97 \pm 0.02) \times 10^{-7}$	$> 10^{13}$
Filament diameter d_f / µm	7	60.0 ± 0.4	-
Filaments per bundle n_f	12k	7	-

[a] data sheet values
[b] measurements on fiber bundles in raw condition (as delivered by supplier)

The hybrid composites (SCFRP) are manufactured using a combination of tape deposition and filament winding technology. Unidirectional layers of pre-impregnated carbon fibers of type Cycom 977-2-35-12KHTS-134 are stacked on a plain steel winding core and wrapped in dry steel fiber bundles. The resin required for steel fiber impregnation originates from the resin excess of the prepreg layers and/or additional resin films of type Cycom 977-2-40, respectively. Pure steel fiber reinforced polymer (SFRP) is prepared by an analogue procedure. As reference material, conventional CFRP is manufactured by an open molding lay-up process. All laminates are cured using autoclave technology at 180 °C and 6.5 bar. The cured hybrid or SFRP laminates are released from the tooling by removing the steel fibers at the end faces of the winding core. By this procedure, multi-layered laminates with different steel and carbon fiber proportions, steel fiber distributions and stacking sequences are prepared. To ensure defined material conditions, all specimens are finally desiccated in a drying oven for 168 hours at a temperature of 50 °C and a pressure of 30 mbar. The microstructure, stacking sequences and

calculated characteristics of the material configurations analyzed in this paper are specified in figure 1.

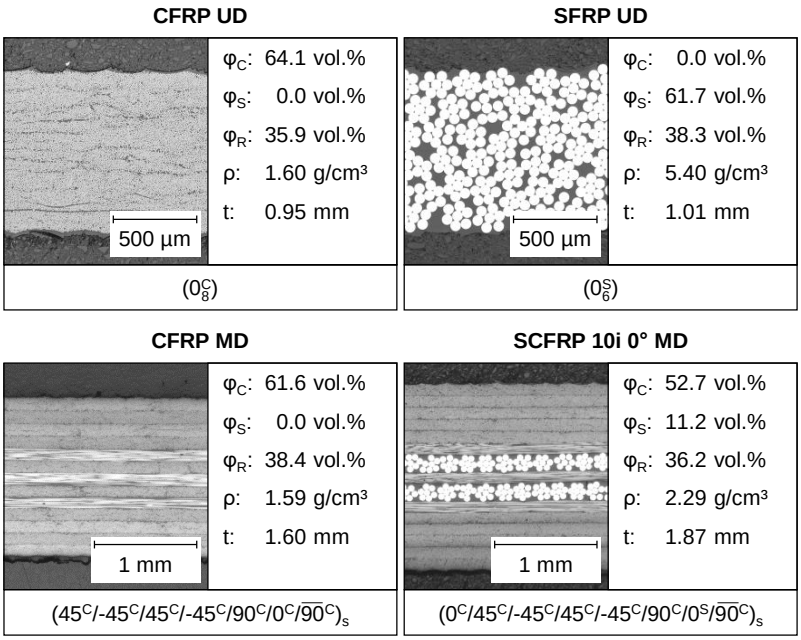

C: Carbon, S: Steel, R: Resin, φ: Volume share, ρ: Density, t: Laminate thickness

Figure 1: Microstructure and calculated characteristics of the analyzed (hybrid) composites

Experimental Characterization

The quasi-static tensile properties of the uniaxial and multiaxial reinforced laminates are experimentally determined. For this purpose, tensile tests are carried out in dependence on DIN EN ISO 527-4 and DIN EN ISO 527-5. The deformation is recorded by a camera system and evaluated by a DIC (digital image correlation) system of type GOM Aramis 4M. For each material configuration, five specimens are tested to failure. Further details are given in [4]. Table 2 summarizes the obtained results.

Table 2: Experimentally determined tensile properties of the laminates

Property	CFRP UD	SFRP UD	CFRP MD	SCFRP 10i 0° MD
Young's Modulus E / GPa	146.1 ± 5.2	136.9 ± 2.9	42.2 ± 0.7	36.7 ± 0.2
Tensile strength σ_{max} / MPa	2492 ± 85	514 ± 7	510 ± 19	597 ± 13
Strain at failure initiation $\varepsilon_{\sigma max}$ / %	1.61 ± 0.06	14.32 ± 0.93	1.23 ± 0.06	1.84 ± 0.06
Ultimate strain at failure ε_{max} / %	1.61 ± 0.06	14.32 ± 0.93	1.23 ± 0.06	11.77 ± 4.95

Both uniaxial and multiaxial reinforced CFRP exhibits a linear-elastic stress-strain relation. Failure occurs occasionally at a nominal strain of 1.61 % or a tensile strength of 2492 MPa in case of CFRP UD and at 1.23 % or 510 MPa in case of CFRP MD. By contrast, the pure steel fiber reinforced composite (SFRP UD) shows a pronounced ductile material performance with a yield strength of 349 MPa, a tensile strength of 514 MPa and an ultimate strain at failure of

14.32 %. The material behavior of the hybrid composite SCFRP 10i 0° MD is characterized by a complex interaction of the brittle CFRP and the ductile SFRP layers. At minor deformation, the hybrid composite exhibits a linear stress-strain relation. After exceedance of a nominal strain of 0.29 %, the integrated steel fibers start to yield, which causes a degradation of the laminate's stiffness. First failure accompanied by a significant load drop occurs at a nominal strain of 1.84 % or 597 MPa. This corresponds to ultimate failure of the 0° and 90° CFRP laminate plies. However, due to the integrated ductile steel fibers, the hybrid composite is able to bear further deformation. During this post-failure stage, four different stress levels can be differed. Both lower stress levels (cf. figure 7) correspond to yielding of the steel fibre reinforced layers. The upper levels relate to deformations of the ±45°-CFRP-layers: Due to the energy absorption capability of the steel fibre plies, the ±45°-CFRP-layers are not completely damaged by the energy release during failure of the 0°-CFRP-layers. In addition, the intact steel fiber plies are able to bypass inter-fibre-failure within the ±45°-CFRP-plies, and thus to include these layers for further load transfer.

Electrical Conductivity

The specific conductance measures a material's ability to conduct electric current. Longitudinal to the fiber direction, an ideal unidirectional continuous fiber reinforced polymer composite can be considered as parallel circuit of several conductors. In this case, the overall conductance is given by the sum of the individual conductance of each conductor. The mean specific conductance in parallel to the fiber orientation κ_1 can thus be calculated by a linear rule of mixtures, considering the volume fraction φ_i and the longitudinal electrical conductivity $\kappa_{1,i}$ of each constituent, eq. 1.

$$\kappa_1 = \sum_i \kappa_{1,i} \cdot \varphi_i = \rho_1^{-1} \qquad \text{(eq. 1)}$$

Perpendicular to the fiber orientation, the composite can be considered as series connection of several conductors. In this case, the overall resistance is given by the sum of the individual resistances of each conductor. The mean specific conductance κ_2 (or κ_3) can then be calculated having regard to the volume fraction and the transverse electrical conductivity $\kappa_{2,i}$ (or $\kappa_{3,i}$) of each constituent, eq. 2.

$$\kappa_2 = \left(\sum_i \frac{1}{\kappa_{2,i} \cdot \varphi_i} \right)^{-1} = \rho_2^{-1} \qquad \text{(eq. 2)}$$

The reciprocal value of the specific conductance is denominated as the specific electrical resistance ρ*, eq. 3.

$$\rho^* = \kappa^{-1} \qquad \text{(eq. 3)}$$

Following this analytical approach, the specific electrical resistance of the laminates is estimated, assuming the specific electrical resistances listed in table 1 and the volume shares listed in figure 1. According to this approach, CFRP UD should demonstrate an electrical conductivity in parallel to the fiber direction of 2.50×10^{-5} Ωm. SFRP UD should exhibit a specific electrical conductance of 0.11×10^{-5} Ωm.

Simulation of the Mechanical Properties

In order to numerically calculate the mechanical properties of the different laminate structures the software GeoDict and especially the modules ElastoDict-LD [7] for the mechanical simulation and ConductoDict for the conductivity simulation are used. Besides modelling microstructures, the software also provides the possibility to import computer tomography (CT) scans and segment the single constituent materials to calculate the material properties directly from the CT scan. Therefore, the software uses voxel based element types.

Modelling the representative volume elements (RVE)

For the CFRP UD and SFRP UD materials two-dimensional RVEs and for the multidirectional CFRP MD and SCFRP 10i 0° MD three-dimensional RVEs are modelled. The two-dimensional models have an element length of 0.5 µm and a size of 1x200x200 elements in x-y-z-direction. The CFRP MD model uses an element length of 0.7 µm and takes the symmetry of the ply stacking into account. The model represents one half of the cross-section and has a size of 100x250x1141 elements. For the SCFRP 10i 0° MD model the same element size as for the CFRP MD model is used. The size is 100x250x1320 elements, again using the symmetry of the ply stacking.

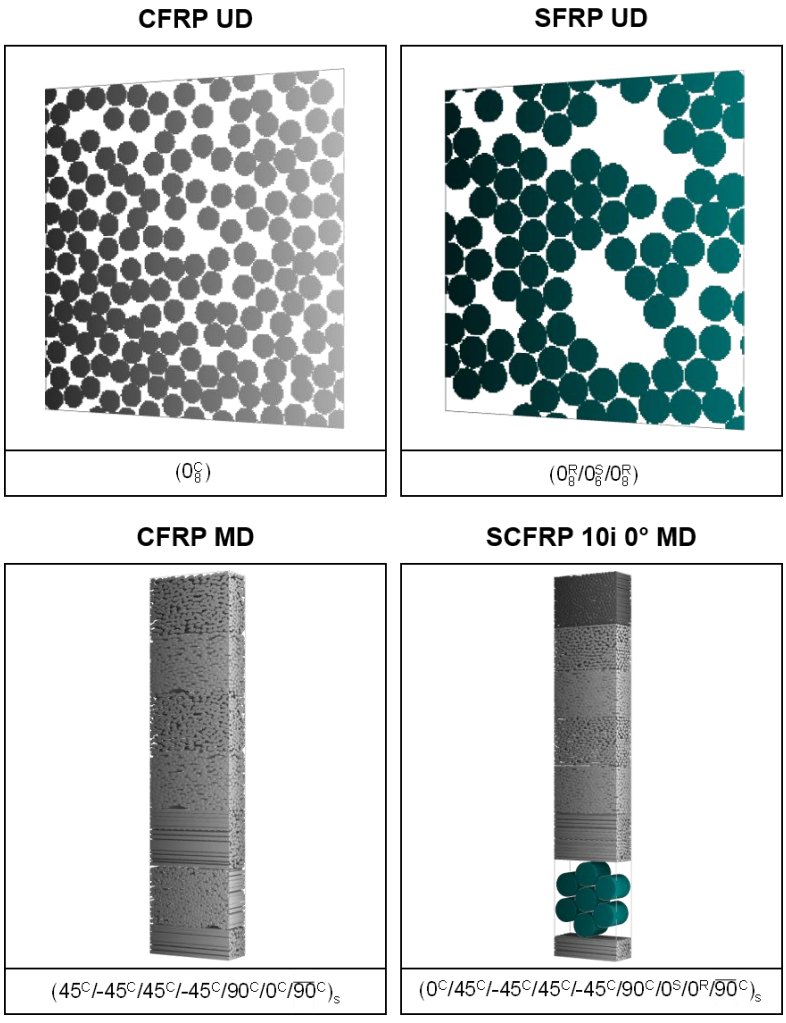

Figure 2: Modelled representative volume elements for the investigated materials

As input the used RVE modelling tool requires the cross-section of the fibers (in this case circular), the solid volume fraction of the different materials (see figure 1), and the fiber direction of the different plies. In the first step of the modeling process, the fibers are cut to the domain allowing an overlapping of the fibers. In the second step, the existing overlap is removed using different morphological manipulations. The algorithm provides three different operations to eliminate the overlap which can be chosen separately: fiber shift, fiber rotation, and fiber deformation. Because the fiber rotation and deformation may have a significant impact on the global fiber orientation and therefore on the mechanical properties of the continuous fiber reinforced material, these two options are disabled and only fiber shifting is allowed. In figure 2 the modelled RVEs are shown.

Modelling the material behavior of the constituent materials

For all three materials, user defined material models (UMATs) are used. The model for the epoxy resin is a linear isotropic material model extended by a damage and failure function. A maximum stress criterion is implemented and the stiffness reduction due to damage (e.g. micro-cracks) follows the function shown in equation (4). Therein ΔC is the stiffness reduction, D is the current damage and the values from T_1 to T_4 are fitting parameters. The damage is calculated as the ratio of the element stress and the ultimate tensile strength from table 1**Fehler! Verweisquelle konnte nicht gefunden werden.**. When failure occurs, the stiffness of the element is reduced to 5 % of the initial value. This value could be smaller, but is a good tradeoff between simulation accuracy and simulation.

$$\Delta C = (T_1 \cdot \log(-T_2 \cdot \log(D)) + T_3) \cdot T_4 \qquad \text{(eq. 4)}$$

Due to their stretching during the production process, carbon fibers exhibit transverse orthotropic material properties. The brittle behavior allows the use of a linear elastic material model with a maximum stress failure criterion. From **Fehler! Verweisquelle konnte nicht gefunden werden.** the stiffness and strength longitudinal to the fiber direction are used. All other values are taken from literature [8] and are listed in table 3.

Table 3: Carbon fiber properties used as simulation input

Property	Value
Transversal Young's Modulus E_2 / GPa	24 (10 % of E_1)
Parallel Plane Poisson Ratio ν_{12}	0.23
Transversal Plane Poisson Ratio ν_{23}	0.1
Shear Modulus G_{12} / GPa	50

The material model for the steel fibers uses an isotropic linear elastic behavior combined with a general von-Mises yield criterion. For the linear elastic part, the Young's Modulus and the Poisson Ratio from **Fehler! Verweisquelle konnte nicht gefunden werden.** are used. Additional an average yield curve from fiber bundle tensile tests is implemented to describe the von-Mises plasticity. In the first step, the stress following the Hooke's Law is calculated. If the calculated elastic stress is greater than the defined yield stress (starting point of the yield curve), the von-Mises stress σ_v for the general load case is determined (using equation 5) and the exact

strain-stress response of the material is calculated by linear interpolation of the yield curve.

$$\sigma_v = \sqrt{\frac{1}{2} \cdot [(\sigma_{11} - \sigma_{22})^2 + (\sigma_{22} - \sigma_{33})^2 + (\sigma_{33} - \sigma_{11})^2 + 6 \cdot (\sigma_{12}^2 + \sigma_{23}^2 + \sigma_{31}^2)]} \quad \text{(eq. 5)}$$

In figure 3 the stress strain curves of the materials models of the different constituent materials are shown. The differences between the stiffness of the materials are clear. While the carbon and steel fiber stiffness is not very different, the stiffness of the epoxy resin is by a factor of about 70 smaller for the undamaged material. This stiffness contrast increases with rising damage up to 1370 which leads to high demands on the stability of the solver. While the material behavior of the carbon fiber and the epoxy resin is quite brittle, the high plasticity of the steel fiber with an elongation at break of about 32 % is apparent.

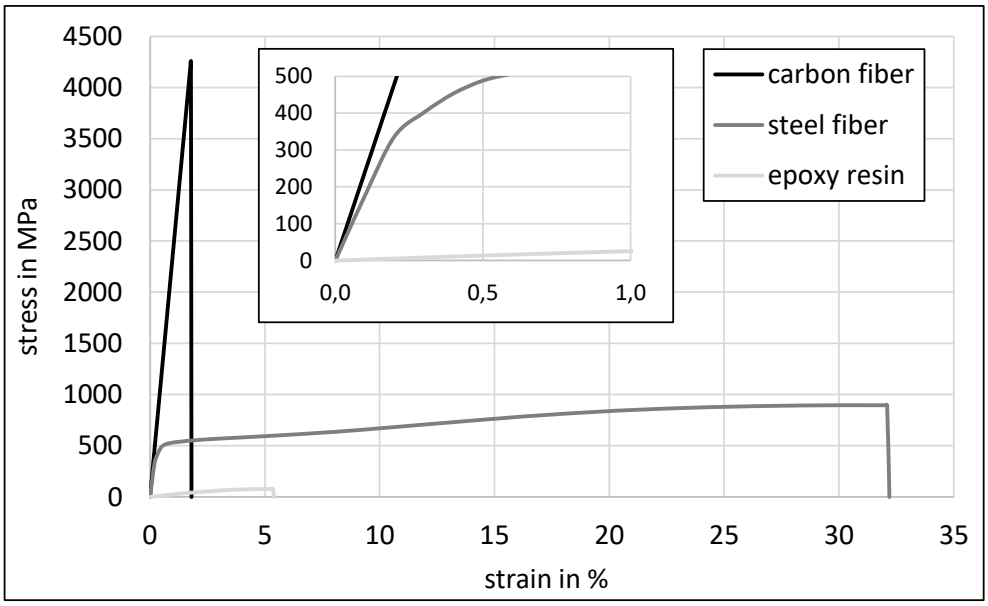

Figure 3: Stress-strain curves of the modelled constituent materials

Simulation results

First the simulation results of the two-dimensional RVE models are discussed in the following section. The simulation of these models is performed defining a uniaxial, path controlled loading. For the simulation 8 CPUs of a 2x10-Core Intel E5-2690v2 @ 3.00 GHz computer are used and the computation time is about 630 s. The used memory is less than 0.3 GB. Figure 4 shows the experimental stress-strain curve for the unidirectional CFRP tensile tests longitudinal (0°) and lateral (90°) to the fiber direction in red. The simulation results are overlaid in black and show very good agreements with the tests regarding stiffness and strength of the material in both loading directions. For the SFRP UD material only tensile tests in fiber direction were performed. The outcome is depicted in figure 5. The experiments show an average strain at failure of 14.3 % which is much lower than the value given by the fiber bundle tests in table 1. As a consequence, the maximum strain parameter for the steel fiber material model was reduced to map the simulation results on the experiments. After the adaption of the

failure criterion the simulation fits the experimental data very well. The linear elastic behavior, onset of yielding, and the stiffness during the yielding agrees well with the tensile tests.

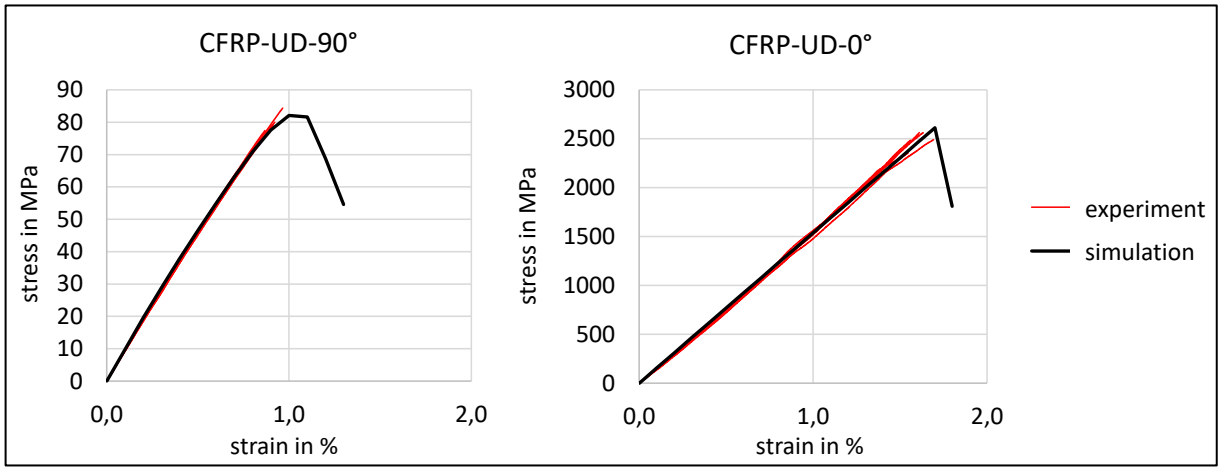

Figure 4: Comparison of the experiment and simulation of CFRP UD tensile tests in longitudinal (0°) and lateral direction (90°)

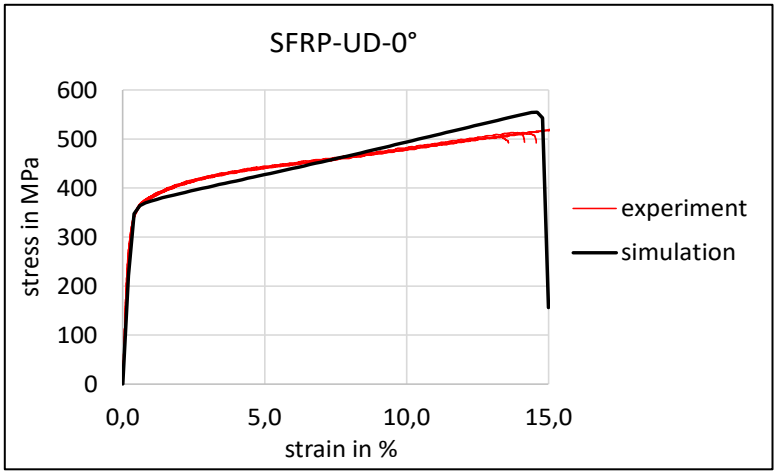

Figure 5: Comparison of the experiment and simulation of SFRP UD in longitudinal (0°) direction

Due to the much higher number of elements of the multidirectional CFRP MD model (approx. 28,500,000 elements) the simulation is performed on the same computer but with 16 CPUs. The computation time is about 20 h and uses 5.5 GB of memory. The results of the tensile tests and the simulation are shown in figure 6. The Young's modulus of the simulated stress-strain curve is 48.1 GPa and the average modulus of the experimental curves is 42.2 GPa. A reason for the deviation of approx. 12 % is the perfect orientation of the fibers in the RVE model. The actual composite exhibits deviations due to the fiber placement resulting from the winding process. However, for the analyzed laminates, the deviation angle is smaller than 0.4° and was thus neglected. This leads to the calculated higher stiffness and strength of the CFRP MD. The calculated strength of 578 MPa differs by less than 12 %.

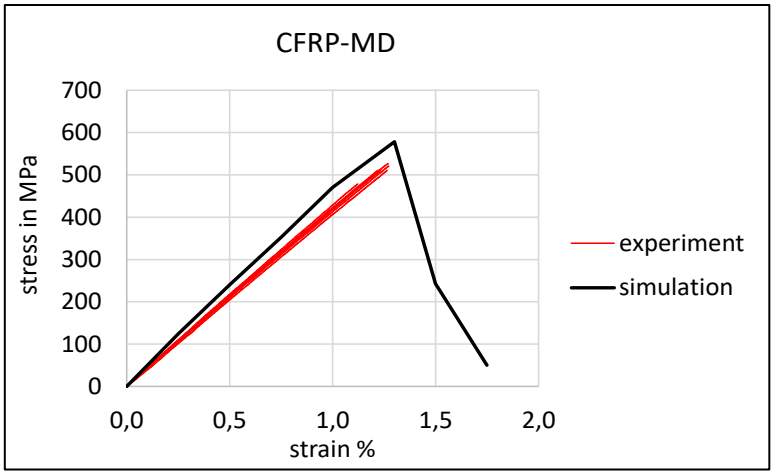

Figure 6: Comparison of the experiment and simulation of CFRP MD in longitudinal (0°) direction

The simulation of the hybrid SCFRP 10i 0° MD material sets high demands on the software, because of the very different material properties already shown in figure 3 and the different fiber diameter scales between the steel (60 µm) and the carbon fiber (7 µm). The experimental stress-strain curves illustrated in figure 7 show a quite complex failure behavior of the hybrid material. In contrast to the CFRP MD material a good-natured post-failure behavior can be detected. At approx. 1.9 % strain the 0°-ply of the laminate fails which leads to a huge drop in the stress-strain curve and the laminate stiffness. After this failure of the main load carrying ply the other carbon fiber plies fail gradually which can be seen in the smaller drops of stress. Due to the high ductility of the steel fibers, this ply is the last to fail. The simulation reproduces the material behavior quite good until the first ply-failure. The stiffness as well as the point of failure of the first ply is in good agreement with the experiments. Again, the stiffness is a little bit higher than in the experiment which can be explained by the disregarded fiber misalignment in the modeling. After the first failure, the stress level of the simulation is too high and the terraced post-failure behavior is not represented in detail. The computation time using 16 CPUs for the SFRP 10i 0° MD model (33,000,000 elements) is 16 h and the used memory 6.5 GB.

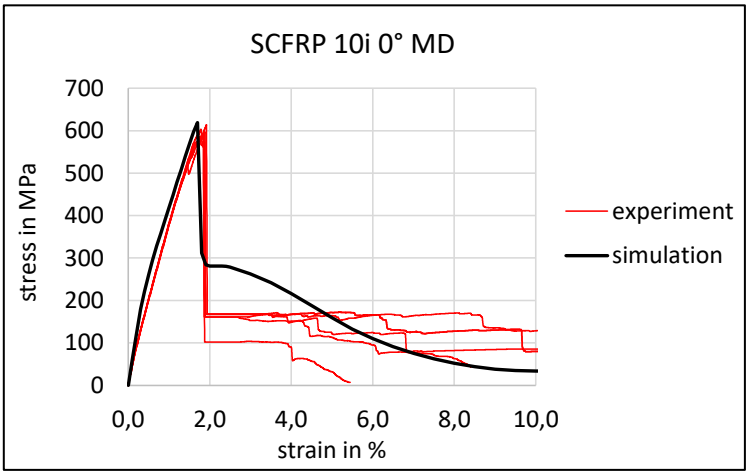

Figure 7: Comparison of the experiment and simulation of SCFRP 10i 0° MD in longitudinal (0°) direction

Simulation of the Electrical Conductivity

For the calculation of the electrical conductivity the same RVE models as for the mechanical simulation are used. As input for the simulation the microstructure and the electrical conductivity of the single constituent materials are needed. The used conductivity properties are listed in table 1. Due to the lack of knowledge about the transverse conductivity of the carbon fibers, the fibers are modeled with isotropic material properties. All simulations are performed on the same computer than the mechanical simulations using 20 CPUs. Because of the high number of CPUs, the calculation times are very short: 15 s for the SFRP UD and CFRP UD model, 202 s for the CFRP MD model, and 112 s for the SCFRP 10i 0° MD model. The result of the simulation is the electrical resistivity of the homogenized material along the main fiber direction (x-direction) and transverse to the fiber direction (y-direction). The resistivity in laminate thickness direction is not calculated, because this value depends strongly on the amount of fiber-fiber contacts – the epoxy resin acts as an isolator – which is not known. In table 4 the calculated resistivity for the different materials and directions are listed.

Table 4: Results of the electrical conductivity simulation

Material	x-direction	y-direction
CFRP UD	2.49×10^{-5}	—
SFRP UD	1.12×10^{-6}	—
CFRP MD	6.27×10^{-5}	4.78×10^{-5}
SCFRP 10i 0° UD	5.67×10^{-6}	5.98×10^{-5}

The results in fiber direction for the CFRP UD and SFRP UD material are in a very good agreement with the analytically calculated resistivity. For the multidirectional CFRP MD the resistivity increases due to the high number of plies which are not directly orientated in the flux direction. The enhancement of the conductivity through the combination of carbon and steel fibers is obvious. The resistivity of the SCFRP 10i 0° UD is approximately one order of magnitude lower than for the CFRP MD.

Discussion

The efforts of micromechanical simulations are on the one hand the reduction of time- and cost-consuming experiments and on the other hand one can get insights into the micromechanics of the material which an experiment cannot provide. The good agreement of the simulated stress-strain curves with the tensile tests already showed the potential of material simulations based on RVEs. The manufacturing of such complex material prototypes is very extensive and could be reduced to a minimum by using micromechanical simulation for the variation of fiber types, laminate stackings or fiber volume fractions.

To understand the functionality and the micromechanical behavior of the material, the visualization of the simulation results for the different load steps is very useful. Figure 8 shows the stress in loading directions for different macroscopic strain-states. At 1 % strain, it is clearly visible that the upper 0°-ply carries most of the load. After the failure of this ply at 1.8 % strain, the stress inside the ply as well as the macroscopic stress drops significantly. In the following steps, the load is carried by the ±45°-plies and the steel fibers.

Figure 9 shows a plot of the UMAT state variable of the damage parameter in the epoxy resin material model. The variable can have values between zero and one, whereas one

equates to failure or total damage of the element. Until the failure of the 0°-ply at 1.8 % strain, the matrix damage mainly occurs in the ±45°- and 90°-plies. After the breakage of the 0°-ply the matrix damage evolves in all plies until at 4.5 % almost the entire matrix is damaged.

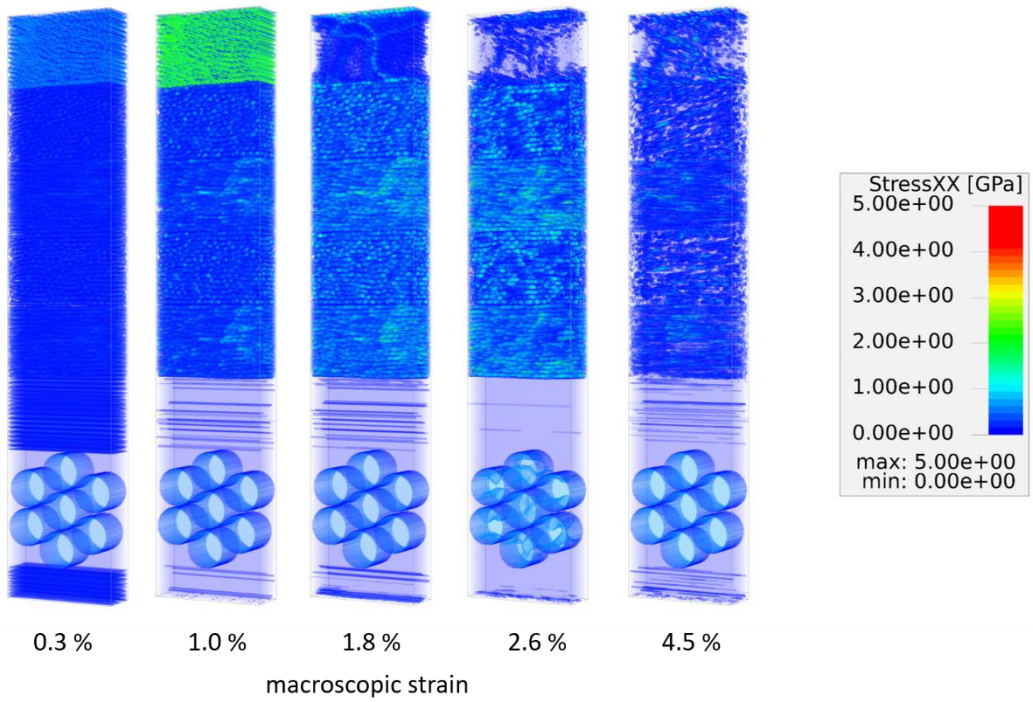

Figure 8: Stress in loading direction (x-direction) for different macroscopic strain-states of SCFRP-10i-0°-UD

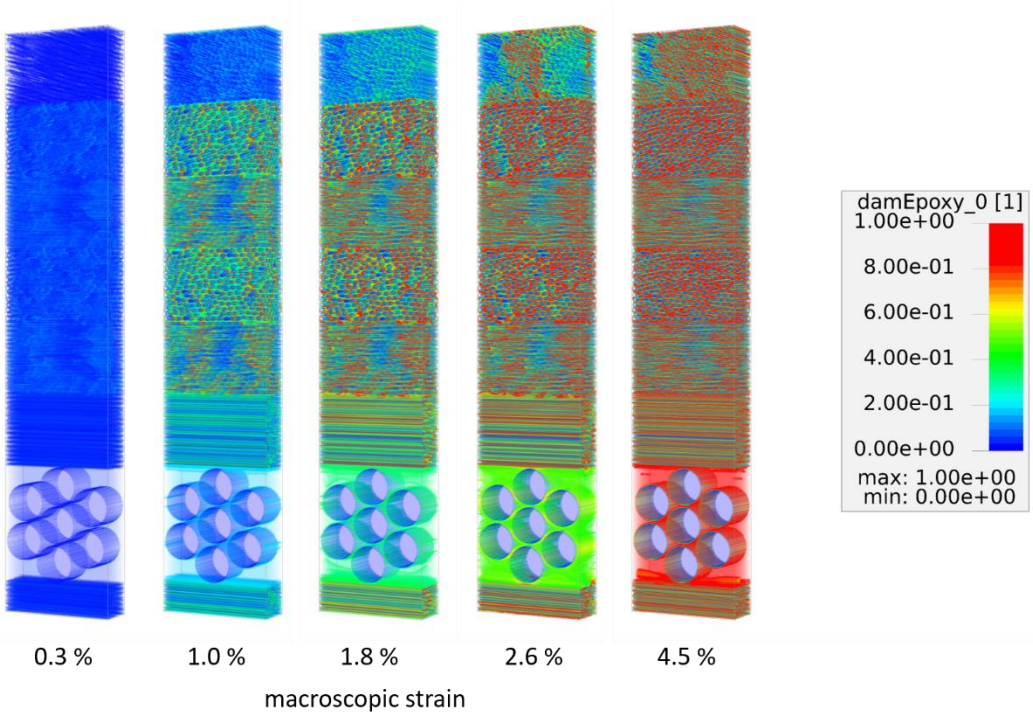

Figure 9: Evolution of the epoxy resin damage for different macroscopic strain-states of SCFRP-10i-0°-UD

In figure 10 the evolution of the failure variable of the carbon fiber material is plotted. The variable can have only a value of zero for a non-failed element or one for a failed element. The plot shows that no carbon fiber failure occurs until the breakage of the 0°-ply. After this instantaneous failure of the load carrying ply, the fiber breakage evolves in the ±45°-plies. Inside the 90°-plies no fiber failure appears, because on the one hand no failure criterion for the transverse direction is defined, but on the other hand the matrix could not transfer enough load to cause a transverse fiber failure, because the matrix elements would fail before.

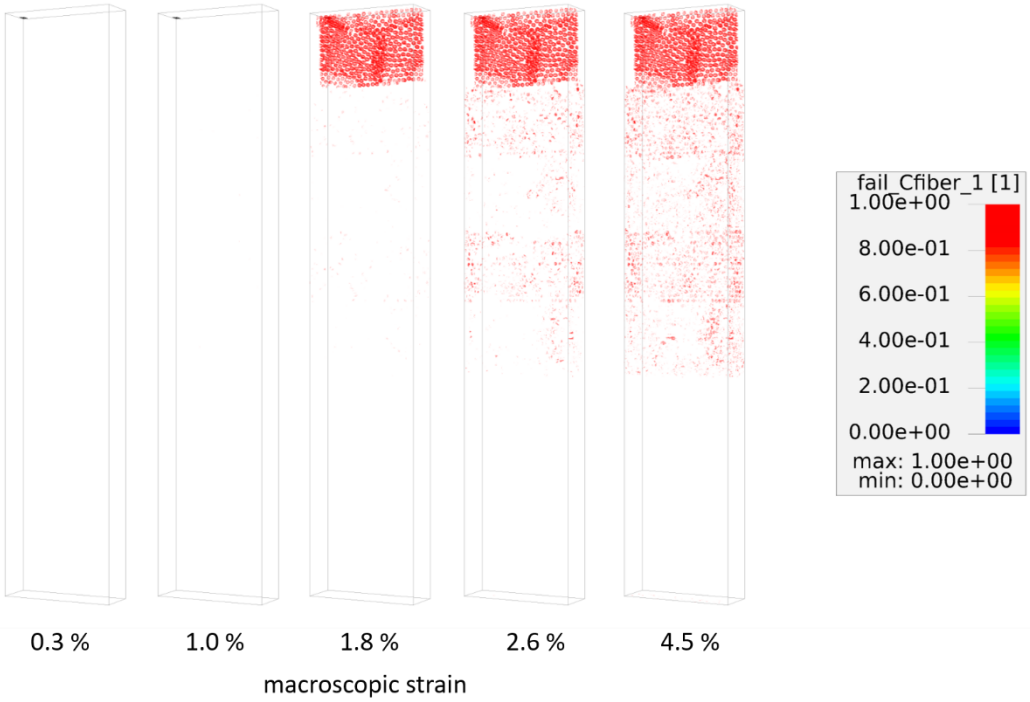

Figure 10: Evolution of the carbon fiber failure for different macroscopic strain-states of SCFRP-10i-0°-UD

Conclusions

Within the present work, a novel hybrid composite consisting of continuous steel and carbon fibers embedded in an epoxy resin is analyzed. The incorporation of ductile steel fibers into CFRP aims to improve both the electrical and mechanical performance of the composite. In this regard, analytical and numerical investigations are performed on unidirectional and multiaxial laminates in order to understand the micromechanical interaction between the individual constituents of such hybrid material in dependence on the load case.

The micromechanical simulations as well as the experiments show an enhancement of the material performance especially in terms of the post-failure behavior and the electrical conductivity. Both the mechanical and conductive simulation shows a very good agreement with test results and could be used for further investigation of the micromechanics of this new hybrid material for a continuously improvement of the material performance. The terraced post-failure behavior of the SFRP 10i 0° MD material could not be reproduced in detail. One reason for that could be that the ±45° layers carrying more load as in the experiment, because no transversal fiber failure is modelled due to the missing of a proper value for the transversal fiber strength. Another reason could be that in this model no fiber-matrix-interface is modelled. The debonding

is represented through the damage variable inside the epoxy resin material model. An additional modeling of the interface could help to reproduce the post-failure behavior more accurate.

Acknowledgements

The financial support of the German Research Foundation (DFG) within the projects BR 4262/2-1 and BA 4073/6-1 is gratefully acknowledged. Prepreg and resin film was kindly supplied by Cytec Engineered Materials GmbH (Östringen, Germany).

Bibliography

[1] Breuer, U. P., “Commercial Aircraft Composite Technology”, Springer International Publishing, 2016.
[2] Garg, C. and Mai, Y. W., „Failure mechanisms in toughened epoxy resins – a review”, Composites Science and Technology, Vol. 31, Iss. 3, pp. 179-223, 1988.
[3] Medina Barron, R. M., “Rubber toughened and nanoparticle reinforced epoxy composites”, IVW Schriftenreihe, Vol. 84, 2009.
[4] Hannemann, B., Backe, S., Schmeer, S.; Balle, F. and Breuer, U. P., “Hybridisation of CFRP by the use of continuous metal fibres (MCFRP) for damage tolerant and electrically conductive lightweight structures”, Composite Structures, Vol. 172, pp. 374-382, 2017.
[5] Toho Tenax Europe GmbH, “Product data sheet for Tenax HTS filament yarn”, Wuppertal, Germany, 2014.
[6] Cytec Engineered Materials, “Cycom 977-2 epoxy resin system – Technical data sheet”, 2012.
[7] Schneider, M., Ospald, F. and Kabel, M., “Computational homogenization of elasticity on a staggered grid”, International Journal for Numerical Methods in Engineering, Vol. 105, pp. 693–720, 2015.
[8] Schürmann, H.: Konstruieren mit Faser-Kunststoff-Verbunden. VDI-Buch. Springer-Verlag Berlin Heidelberg, Berlin, Heidelberg, 2007.